Natural Resources Research, Vol. 32, No. 2, April 2023 (© 2023)
https://doi.org/10.1007/s11053-023-10161-z

Original Paper

Combining Automated Mineralogy with X-ray Computed Tomography for Internal Characterization of Ore Samples at the Microscopic Scale

Florian Buyse,[1,4,6] **Stijn Dewaele**,[2] **Matthieu N. Boone**,[3,4] **and Veerle Cnudde**[1,4,5]

Received 12 July 2022; accepted 7 January 2023
Published online: 19 January 2023

Advanced chemical and mineralogical techniques are necessary to further our understanding of ore deposits and their genesis. Using X-ray micro-computed tomography (μCT) and an automated mineralogy (AM) system based on scanning electron microscopy with an energy-dispersive X-ray spectrometer (SEM–EDX), we investigated the internal mineralogy of Sn–Nb–Ta pegmatites. This paper presents a comprehensive methodology to quantify and visualize the mineral relationships of ore samples in three-dimensional space at the microscopic scale. A list of all possible minerals present, a so-called mineral library, was deduced with a SEM-based AM system and served as the ground truth for the interpretation of μCT data. A reconstructed attenuation coefficient (μ_{rec}) was calculated for mineral phases that have been identified and provided a most correct guidance to differentiate between minerals for a given experimental μCT setup. Despite some limitation in sample size and mineral identification, these complementary techniques enabled the differentiation of a Fe–Li mica from biotite based on the chemical attribution of lithium to μ_{rec}. Using statistical descriptors, we quantified the general orientation of individual mineral phases and their spatial correlation to comply with the needs of processing large datasets at a low computational expense. Applying this comprehensive methodology to a case study demonstrates the possibilities of combining a SEM-based AM system with μCT analysis to investigate ore samples at the microscopic scale.

KEY WORDS: X-ray computed tomography, Automated mineralogy, Mineral texture, Correlative microscopy, Pegmatites.

[1]Pore-Scale Processes in Geomaterials Research Group (PPro-GRess), Department of Geology, Ghent University, Krijgslaan 281/S8, 9000 Ghent, Belgium.
[2]Laboratory for Mineralogy and Petrology, Department of Geology, Ghent University, Krijgslaan 281/S8, 9000 Ghent, Belgium.
[3]Radiation Physics Research Group, Department of Physics and Astronomy, Ghent University, Proeftuinstraat 86/N12, 9000 Ghent, Belgium.
[4]Centre for X-Ray Tomography (UGCT), Ghent University, Proeftuinstraat 86, 9000 Ghent, Belgium.
[5]Environmental Hydrogeology, Department of Earth Sciences, Utrecht University, Princetonlaan 8a, 3584 CB Utrecht, The Netherlands.
[6]To whom correspondence should be addressed; e-mail: florian.buyse@ugent.be

INTRODUCTION

In this ever-changing world, we are more and more confronted with the challenges of future mineral supply to an accelerating global population growth (Ali et al., 2017). In addition, modern society relies increasingly on the development of renewable energy sources and other high technology applications that require not only a vast amount of common commodities (e.g., copper, steel), but also a growing number of critical low-volume elements (Hayes & McCullough, 2018; Wellmer et al., 2019). Detailed

characterization of the morphology, texture, mineralogy, and chemistry of different desirable minerals, as well as the bulk minerals in which they are embedded, plays an important role in the optimal recovery of critical raw materials (Reuter et al., 2019).

Mineralogical studies of ore deposits conventionally rely on macroscopic observations of hand specimens collected during fieldwork and on microanalytical two-dimensional (2D) techniques to characterize the chemical, mineralogical, and structural variations of millimeter- to centimeter-sized samples, at a spatial resolution down to the microscopic scale (Pearce et al., 2018). Microscopic observations are often limited to optical microscopy and different microbeam analytical techniques, combined with integrated imaging techniques like scanning electron microscopy (SEM). SEM is often assisted by 2D elemental mapping using energy-dispersive (EDX) or wavelength-dispersive (WDX) X-ray spectrometers or complemented with data from an electron probe microanalyzer (EPMA) acting as an analytical tool to determine non-destructively the chemical composition of small volumes of solid materials (Reed, 2005). SEM may also be combined with a focused ion beam (FIB–SEM) for serial FIB milling of the sample surface to acquire a sequence of cross-sectional SEM images and thus a three-dimensional (3D) visualization of a sample (Gu et al., 2020). Often, additional structural and analytical chemical methods, such as X-ray diffraction (XRD) and X-ray fluorescence (XRF), are used to determine the mineralogical and chemical composition of samples.

Although the above-mentioned techniques are well-known and commonly used for the characterization of geological samples, there is a need for non-destructive characterization that provides in 3D the structural, mineralogical, and chemical composition of the interior of geological samples (Wang & Miller, 2020). Accurate 3D mineralogical and geochemical characterization is crucial for improving the understanding of ore genesis (Godel, 2013), and it is particularly applicable to petrological and genetic investigations of low-grade fine-grained ore deposits or nugget-type of mineralization (Kyle & Ketcham, 2015). These motivate the need for the development of new and innovative technologies for adequate ore characterization (Becker et al., 2016; Gessner et al., 2018) and associated data analysis (Guntoro et al., 2019a).

X-ray micro-computed tomography (μCT) is a non-destructive X-ray imaging technique that allows for the analysis of the interior of geological samples in 3D. This technique has the ability to eliminate stereological errors from conventional 2D image analysis and to leave samples intact for further sample characterization (Guntoro et al., 2019a). This offers the possibility to study mineral relationships in 3D (e.g., Jardine et al., 2018) and to acquire quantitative estimates of mineral shape, size, and orientation (e.g., Ketcham & Mote, 2019). The principle of μCT is based on the calculation of the X-ray linear attenuation coefficient (μ_{lin}), which depends on material properties (effective atomic number, density) and the incident energy of an X-ray beam. Typical geological sample sizes for μCT imaging measure between 1 mm and 5 cm (Cnudde & Boone, 2013), where a trade-off has to be made between the transmitted X-ray photon flux and resolution. The application potential of this technique has been reviewed within geosciences (Cnudde & Boone, 2013; Kyle & Ketcham, 2015; Wang & Miller, 2020) and has established its contribution to geological studies. Processed μCT data provide images of mineral relationships in 3D together with statistical parameters that are of interest for studies of ore-forming processes, extractive metallurgy, and metal production engineering (Pearce et al., 2018; Wang & Miller, 2020). Because the main drawback of standard μCT is the absence of chemical information, it is currently only possible to segment various compounds based on different X-ray attenuation and/or shape properties (Guntoro et al., 2019a).

Despite continuous technological and computational advances (Wang & Miller, 2020), most applications in mineral characterization are rather limited to the 3D segmentation of major phases, i.e., pores, low-density phases, and high-density phases (Guntoro et al., 2019a). Therefore, recent work in μCT focuses on the development of image post-processing procedures (Becker et al., 2016; Guntoro et al., 2019b), whether or not together with complementary microscopic techniques (De Boever et al., 2015; Laforce et al., 2016; Reyes et al., 2017; Warlo et al., 2021), to differentiate between complex intergrown mineral phases. In future, the integration of machine learning and artificial intelligence is considered to be crucial for the generation of mineralogical information from standard μCT data (Guntoro et al., 2019a). Various techniques have been developed to extract mineral features from

μCT datasets (Jardine et al., 2018). Existing techniques are, however, currently limited to the computational expense of processing large datasets (Guntoro et al., 2019a) and are just now slowly starting to emerge (e.g., Strzelecki et al., 2021).

This study aimed to develop a comprehensive methodology by combining state-of-the-art μCT and an SEM-based automated mineralogy (AM) system to characterize the mineralogy of ore samples in 3D. We present a test study on pegmatite-hosted Sn–Nb–Ta mineralization in the Mesoproterozoic orogenic belts of Central Africa (Dewaele et al., 2011; Melcher et al., 2015), where we overcame some of the traditional issues to characterize the internal geochemical and mineralogical composition in 3D at the microscopic scale.

MATERIALS AND METHODS

Samples

Samples were selected from the intensively studied Sn–Nb–Ta mineralization of the Gatumba area in western Rwanda, Central Africa (Lehmann et al., 2008; Dewaele et al., 2011; Hulsbosch et al., 2013; Lehmann et al., 2014; Hulsbosch & Muchez, 2020). This mineralization consists of millimeter-sized cassiterite and columbite–tantalite minerals hosted within much less dense gangue minerals (mainly quartz, feldspars, and muscovite) (Dewaele et al. 2011). In an individual pegmatite, a mineralogical and geochemical zonal development is observed from margin toward the center, with a hydrothermal overprint completely altering the original pegmatite composition at some locations (Dewaele et al., 2011; Hulsbosch & Muchez, 2020). The exact spatial relationship between the different ore minerals is difficult to observe with standard techniques, and thus not known.

In addition to representative polished sections with higher concentration of ore minerals for reflected light microscopy and SEM-based AM analyses, rock samples were prepared specifically for μCT analysis. Because cylindrical samples have the most efficient geometry for the cone-beam configuration employed in most modern laboratory μCT systems (Kyle & Ketcham, 2015), drilled core samples were made (2 cm in diameter). These drilled core samples were afterward also prepared to be suitable for further analyses with optical microscopy and SEM-based AM (i.e., polishing of top and bottom surfaces). Results are discussed by means of two representative cylindrical samples A and B acquired from one of the pegmatite samples from the Gatumba area, of which sample A was used as an example to discuss the process of 3D mineral phase segmentation and feature extraction.

Optical and Scanning Electron Microscopy

Reflected light microscopy was carried out at Ghent University, using a Nikon Eclipse LV100N POL polarizing petrographic microscope, as a preliminary step to identify Sn–Nb–Ta–(W)-bearing ore minerals and their interrelationships (e.g., identification of possible mineral inclusions). SEM–EDX was performed at Ghent University using TESCAN Integrated Mineral Analyzer (TIMA-X) equipped with a field emission gun and one EDX detector. TIMA-X is a system optimized to rapidly acquire low-count spectra (Hrstka et al., 2018) and it combines calibrated back-scattered electron (BSE) imaging and EDX analysis for mineral classification training using an AM system. The mineral distribution maps were based on the comparison of EDX spectra obtained from each pixel with a classification scheme, where a set of rules were designated to the calibrated line intensities of the different elements (see also Hrstka et al., 2018). The working conditions were: an acceleration voltage of 25 kV, a working distance of 15.0 mm, and a spatial resolution between 9 and 18 μm for both BSE images and EDX spectra. The energy resolution of the EDX spectra, as measured at Mn Kα, was ± 140 eV. The acquired mineralogical information served as a mineral library for the interpretation of the μCT data.

X-ray Micro-Computed Tomography (μCT)

The μCT analyses were performed at the Ghent University Centre for X-ray Tomography (www.ugct.ugent.be). The High-Energy CT system Optimized for Research or HECTOR (Masschaele et al., 2013) was used under the scanning conditions as summarized in Table 1. Reconstructions of the projectional radiographs, acquired using the traditional cone-beam μCT setup, were performed with the Octopus reconstruction software (Vlassenbroeck et al., 2007). This software tool allows for pre-processing corrections (e.g., flat field correction and ring filter) and

Table 1. Experimental setup of μCT scans

Voltage	120 kV
Power	10 W
Projections	2400
Filter	Al 1 mm
Exposure time	1000 ms
Spatial resolution	18 μm

corrections during the reconstruction (e.g., beam hardening correction). Image analysis was executed in the Fiji/ImageJ software (Schindelin et al., 2012) using a 3D trainable Weka Segmentation plugin (Arganda-Carreras et al., 2017) for the mineral phase segmentation and by using executable scripts to automate certain repetitive steps. The different steps that were undertaken to investigate the different mineral phases in 3D are discussed below and summarized in Figure 1.

Information about the mineralogical composition was obtained during optical microscopy and TIMA-X analyses of the polished sections and was supplemented by observations from previous research (Lehmann et al., 2008; Dewaele et al., 2011; Hulsbosch et al., 2013; Melcher et al., 2015; Hulsbosch & Muchez, 2020). The mineralogical composition, material density (ρ), and X-ray energy determine the linear attenuation coefficient (μ_{lin}) and provide insight into the capability of μCT to segment minerals with similar attenuation (Fig. 2a). However, in laboratory-based μCT, a polychromatic source is used and the energy dependency of μ_{lin} needs to be taken into account. Therefore, the theoretical μ_{lin} was recalculated for the given experimental setup (Table 1) using the in-house developed software Arion (Dhaene et al., 2015). This value was hereafter referred to as the reconstructed attenuation coefficient (μ_{rec}). The calculations of μ_{rec} took into account the spectral sensitivity of the detector and the effects (e.g., metal artifacts and beam hardening) induced by the polychromaticity of the X-ray source. Therefore, properties like sample size, shape, elemental composition and density were taken into account in the simulation tool. For a given setup, μ_{rec} serves as a more accurate depiction of the possible segmentation between the different mineral phases (e.g., μ_{rec} of schorl and apatite was here too similar to be segmented using this setup; Figure 2b) and the interpretation of the different mineral interrelationships.

Despite measures taken to prevent imaging artifacts (e.g., Al filter, beam hardening corrections during the reconstruction), and thus to eliminate μ_{rec} variability, the final μCT image vertically still displayed variable grayscale values throughout the slices for the same mineral phase (see also Fig. 3 in Guntoro et al., 2019b). A region of interest, including more than 80% of the dataset, was selected to avoid mineral phase segmentation issues.

Because μCT images contain numerous mineral phases and, thus, numerous gray values (Fig. 3a), prior noise filtering was not considered, as the variance was also taken into account during the segmentation step (see below). As a first step of data preparation, automatic thresholding of the data was performed with Otsu's method (Otsu, 1979) to separate the background from sample data. This was followed by a four times 1-pixel erosion operation (binary morphology) to avoid false segmentation at the sample borders that could not be resolved with beam hardening corrections (Fig. 3b). Segmentation was then performed using Weka 3D segmentation (Arganda-Carreras et al., 2017) within the Fiji environment, where a set of 50 images was used to train the following features: edges (canny edge detection) and texture filters (mean, variance) in a fast random forest classifier. The training of the classifier was adopted iteratively by using input from corresponding mineral distribution maps acquired with TIMA-X until an accurate segmentation result was achieved on the subset (Fig. 3c). The trained classifier was then used to segment automatically each corresponding dataset (over 1000 images each). A tiling algorithm, reducing the memory requirements (Arganda-Carreras, 2018), was applied to prevent running into out-of-memory exceptions when processing large 3D datasets (> 3 GB) on a regular desktop. Previously, this algorithm has already been successfully used in, e.g., Callow et al. (2020). Post-processing steps were undertaken for each individual segmented phase to avoid partial volume effects at boundaries between two segmented phases (Fig. 3d). A boundary between a high-density phase and a low-density phase would be incorrectly interpreted as an intermediate density phase and was therefore removed from the data using binary morphology operations (see detailed excerpts in Fig. 3e–g).

Feature Extraction

Segmentation of the μCT images resulted in a dataset of labeled images, where each label represented the 3D volume of a segmented phase. To

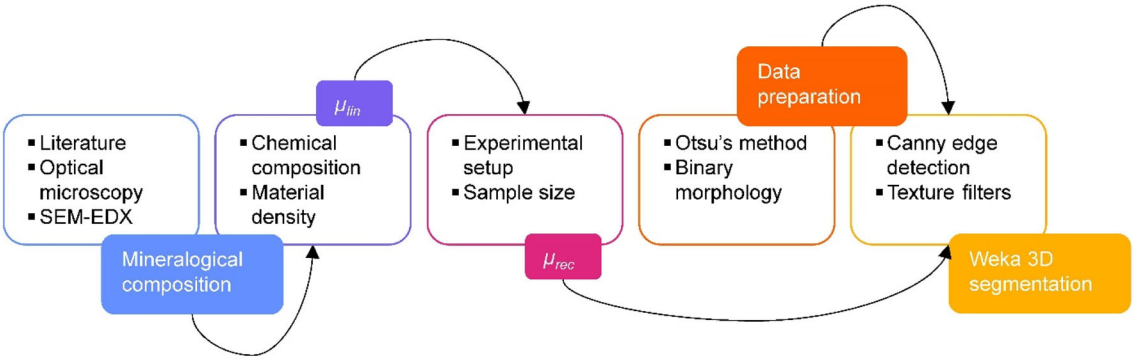

Figure 1. Overview of the different steps that were undertaken for the segmentation of different mineral phases.

represent the interrelationships between two different segmented phases, the Pearson correlation coefficient was calculated, thus:

$$\rho(X,Y) = \frac{\mathrm{cov}(X,Y)}{\sigma(X)\sigma(Y)} \quad (1)$$

This measure is the ratio of the covariance of two variables to the product of their standard deviations. For two phases X and Y (Eq. 1), metrics are calculated using the surface areas of two phases, which are compared along a defined direction (see below) and are normalized to the total area of a sample within each 2D slice (which translates as a comparison of area percentages). Values of the Pearson correlation coefficient range between − 1 (negative linear correlation) and 1 (positive linear correlation). A correlation coefficient of 0 implies no linear dependency between two phases in that direction.

The coefficient of variation (Eq. 2) was then calculated to represent the general orientation of each individual segmented phase, thus:

$$c_v = \frac{\sigma}{\mu} = \frac{\sqrt{\sum_i (x_i - \mu)^2 p(x_i)}}{\mu} \quad (2)$$

This measure is the ratio of the standard deviation (σ) to the mean (μ) of the previously mentioned area percentages calculated along a defined direction. This measure is dimensionless and is thus of interest for comparing numerical values of different populations with various averages. The interpretation of the data was based on the fact that higher values are obtained along the longitudinal axis of a phase and lower values are obtained perpendicular to this axis (see Fig. 4). Phases that have no preferential elongation/orientation display similar (low) values for each measured direction.

As previously mentioned, the above statistical measures were calculated along a defined direction. Images were usually stored as a stack of virtual 2D slices perpendicular to the rotational axis or Z-axis, but calculations for the 2D slices along the Z-axis only give 1D information. For a stereographic depiction of a possible variety in statistical measures along different predefined directions, and thus in 3D, the images were re-sliced along all possible directions. Orientations were presented in a spherical coordinate system using the azimuth on the XY plane and the inclination from the Z-axis (Fig. 5a). Using a spacing of 15° along the azimuth on the XY plane (360°) and the inclination from the Z-axis (90°) gave 175 predefined directions. A script was written in Fiji/ImageJ to re-slice automatically the images over all predefined directions and to calculate along each defined direction the surface areas for each segmented phase. Data were represented correspondingly in a polar rose chart using Plotly Python Open Source Graphing Library (Fig. 5b).

RESULTS

Mineral Distribution Maps

The mineral content of the drilled core samples (based on mineral distribution maps acquired with TIMA-X and sorted according to μ_{rec}; Fig. 2b) consisted of kaolinite, beryl, albite, quartz, K-feldspar, muscovite, Fe–Li mica, schorl, apatite, zircon, barite, and columbite–tantalite. The matrix occurring between the larger-sized minerals of these samples consisted almost entirely of quartz and albite, but often contained traces of K-feldspar occurring together with beryl. Muscovite was next to

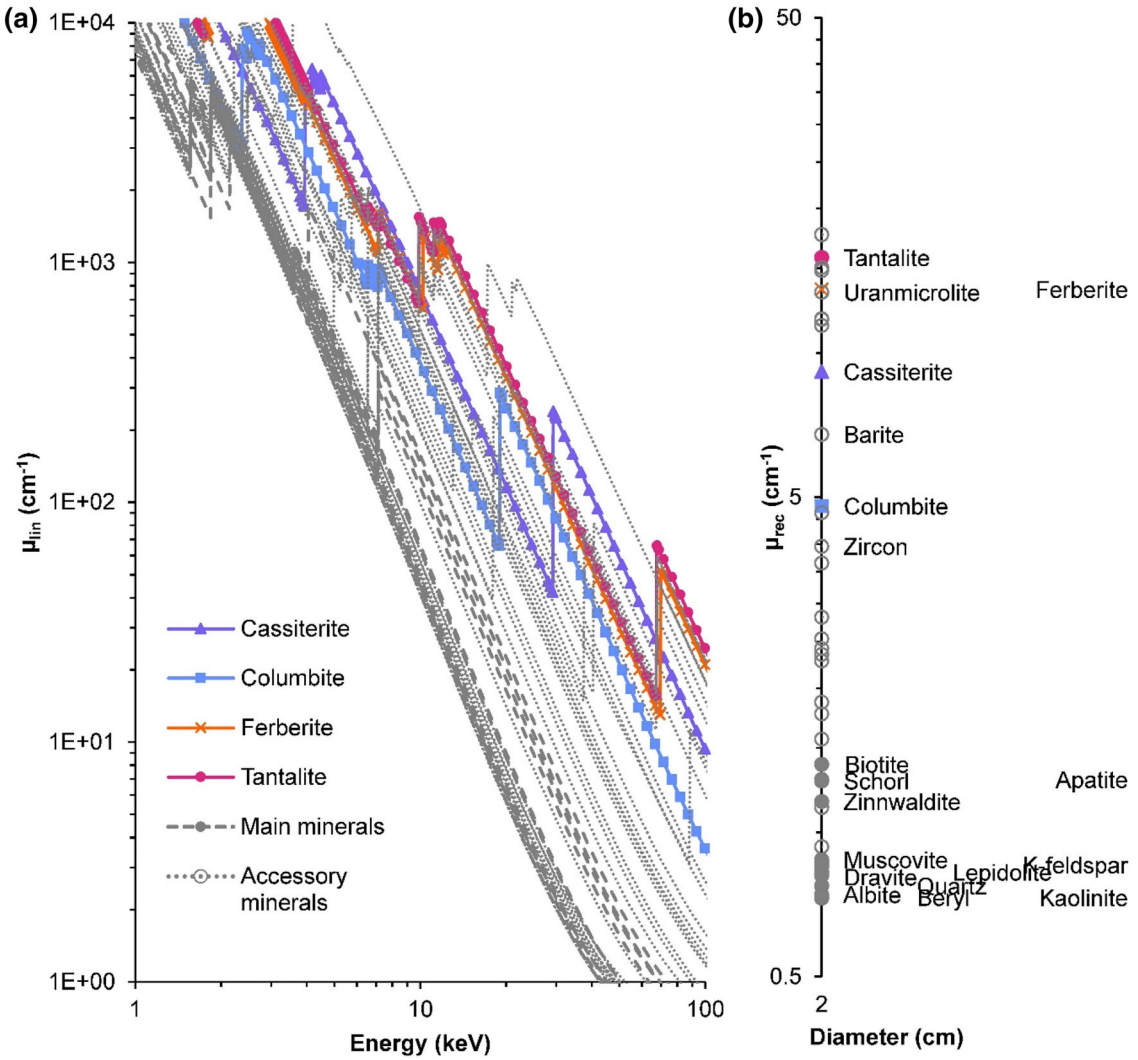

Figure 2. Calculated attenuation coefficients of all minerals possibly present. (**a**) Linear attenuation coefficients (μ_{lin}) of the studied mineral assemblages as a function of X-ray energy. (**b**) Reconstructed attenuation coefficients (μ_{rec}) as calculated for the given experimental setup and sample size. The FFAST database maintained by the National Institute of Standards and Technology (NIST) (Chantler et al., 2005), and available online at physics.nist.gov/PhysRefData/FFast/html/form.html, allows to calculate μ_{lin} as a function of energy. Density values for the different mineral phases are derived from the calculated densities in the handbook of mineralogy (Anthony et al., 2001) and is available online at handbookofmineralogy.org.

quartz and albite an important constituent and it was observed to be often overgrown by an albite matrix (Fig. 6b). Muscovite ranges in size from centimeter-size to aggregates of submillimeter-sized crystals. Kaolinite was closely associated with muscovite, but was only present in minor amounts. Besides muscovite (Fig. 7a), another mica was present to a much lesser extent and has been identified as Fe–Li mica (Fig. 7b). Tourmaline occurs as grouped acicular crystals. EDX analyses of tourmaline showed significant amounts of Fe, Al, and to a lesser extent Na and Mg. Therefore, tourmaline was identified as a Fe-rich member of the schorl–dravite series (cf., Hulsbosch et al., 2013). Apatite mostly occurred as dispersed submillimeter-sized minerals within the matrix. One of the investigated polished sections of sample A rather displayed a grouped occurrence of apatite grains (Fig. 6b). Barite was observed as a small veinlet (400 μm) along the cleavage planes of muscovite and also as an inclusion within tourmaline. Small columbite–tantalite inclusions (18 μm) were observed in both the albite–quartz matrix and in association with muscovite grains. Cassiterite was not observed during TIMA-X mapping.

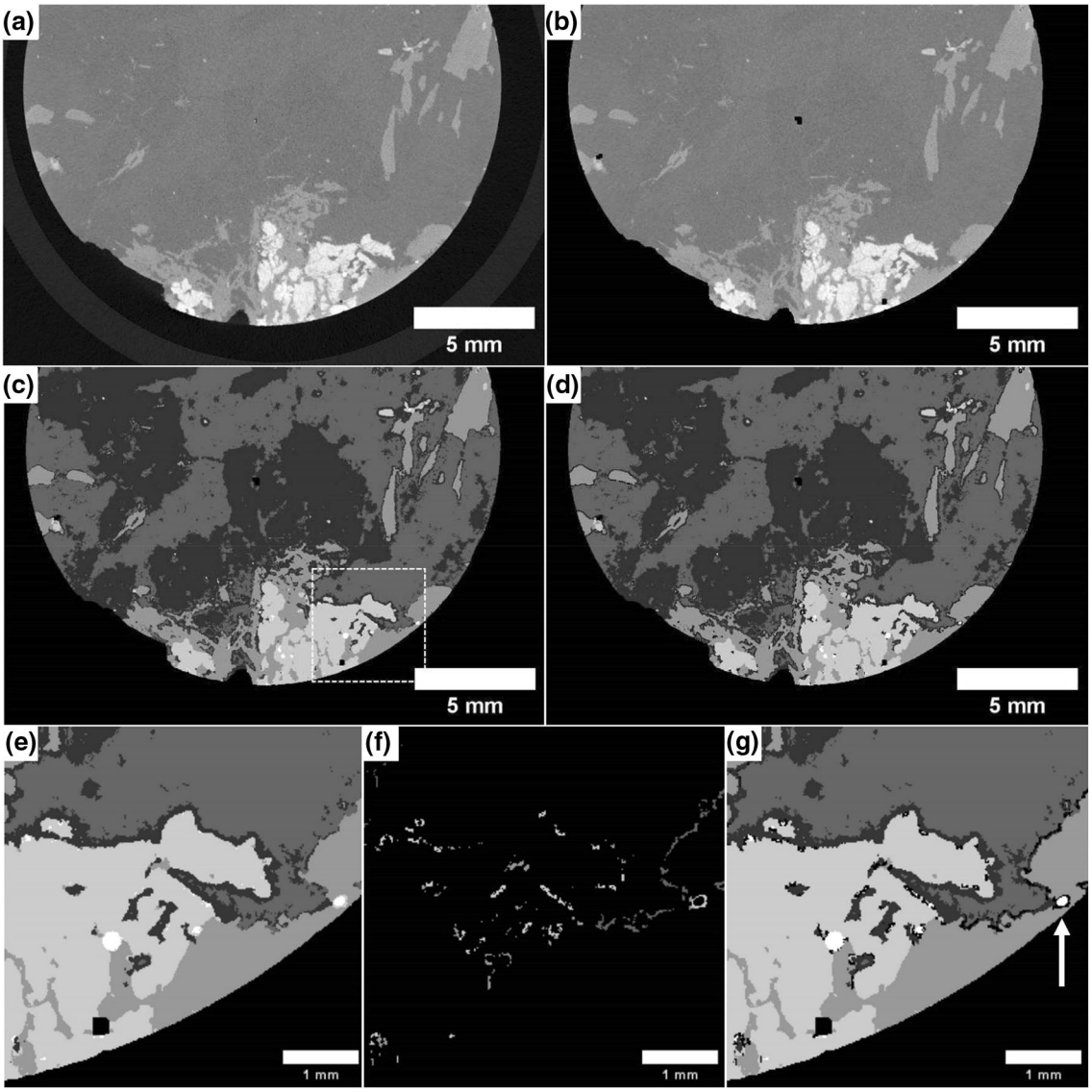

Figure 3. Procedure of post-processing the segmented μCT data. (**a**) Original μCT slice where lighter gray values correspond with higher μ_{rec} values. (**b**) Data preparation by automatic thresholding and binary morphological operations. (**c**) Mineral phase segmentation using Weka 3D segmentation. (**d**) Segmented dataset after post-processing. (**e**)–(**g**) Detailed excerpts (see **c**) of how intermediate mineral phases are removed from the segmented dataset. (**f**) Removed datapoints of where an intermediate phase coincides with the area overlapped by both the low-density phase and high-density phase after a single dilation (morphological operation). (**g**) Final segmented image where misclassified intermediate phases (see, e.g., removed rim of intermediate phase around high-density phase) are excluded for further feature extraction.

X-ray Micro-Computed Tomography (μCT)

Comparison of Mineral Distribution Maps with μCT Data

The μCT images of the drilled core samples (Fig. 6d) were interpreted by comparison with the equivalent mineral distribution maps acquired with TIMA-X (Fig. 6b) and by using the calculated μ_{rec} values of the occurring minerals for the given experimental setup (Fig. 6c). The matrix of the samples consisted almost entirely of two phases that were close to each other in grayscale values, but were still visually distinguishable based on slight differences in grayscale values (Fig. 8a). These mineral phases were identified as quartz and albite

and they occurred as interconnected phases throughout the drilled core samples. The next main mineral phase identified in the μCT data was muscovite. It occurred as large centimeter-sized scaly mineral fragments, but also as much smaller fragments (often as stellate aggregates) disseminated in the matrix. It was often observed for the large scaly muscovite fragments that they were overgrown by a small border of albite matrix, regardless of being located within a quartz-rich matrix. Some of the larger muscovite fragments were altered and only displayed relicts of the original shape. K-feldspar was, similar to observations with TIMA-X, found to be associated with beryl within the samples (Fig. 8a). Euhedral crystals of K-feldspar and beryl were observed only when occurring with(in) muscovite and/or neighbored by schorl. Apatite occurred mostly as a minor phase, but was widely distributed throughout the samples. Together with TIMA-X observations (see also Fig. 6), it was observed that apatite may occur as well as grouped fragments that were strongly intergrown with stellate aggregates of muscovite. Minor occurrences of dense minerals, which appeared to be mainly zircon grains, when compared with corresponding mineral distribution maps, were strongly correlated with these grouped occurrence of apatite grains. The prismatic/acicular crystal habit of schorl (Fig. 8a) allowed to differentiate these mineral fragments from apatite. Schorl was unaffected by the presence of other mineral phases and maintained its mineral shape. Clusters of schorl fragments are unobstructed

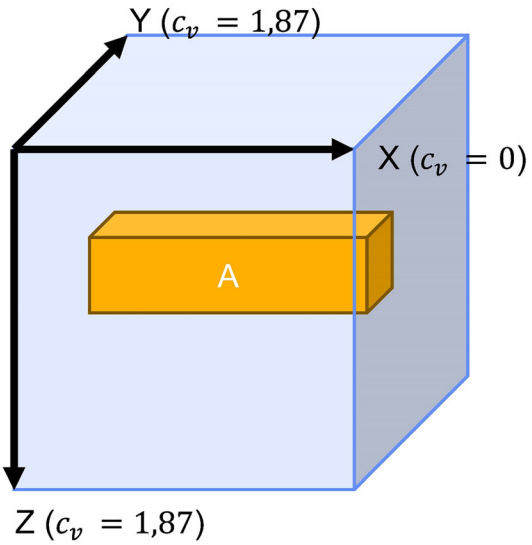

Figure 4. Virtual sample (X:Y:Z = 9 × 9 × 9) containing a segmented phase A (9 × 2 × 2). The coefficient of variation is 0 for phase A when measured along the X-axis (as the values of A remain constant, i.e., Y:Z = 2 × 2), while the coefficient of variation is 1.87 for phase A when measured along the Y- or Z-axis (i.e., the measured values are here either 0 or 9 × 2).

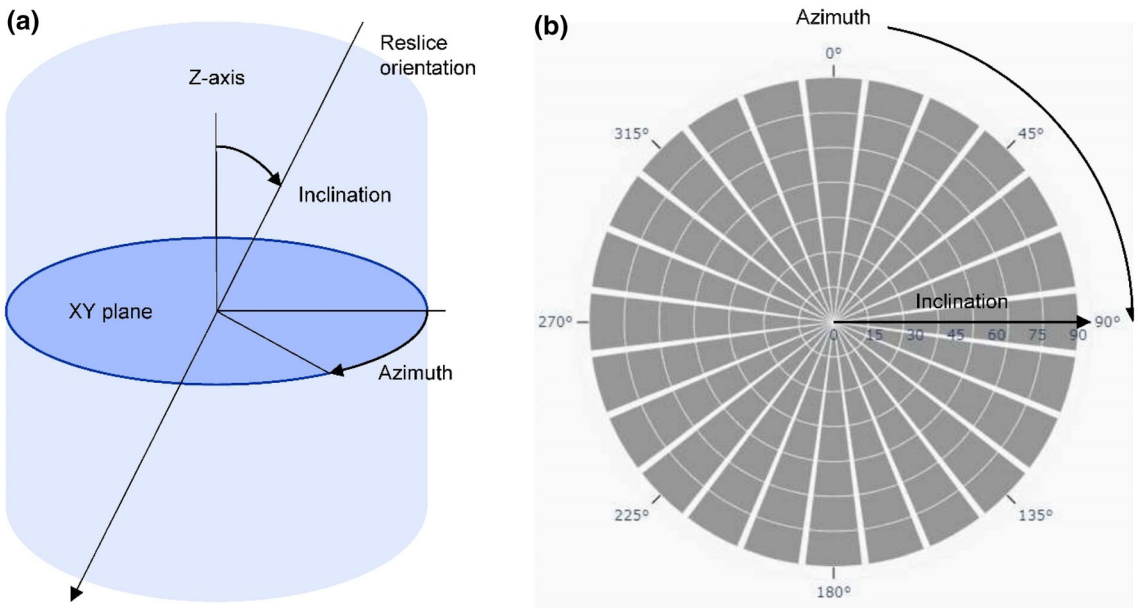

Figure 5. Outline for visualization of oriented statistical measures. (**a**) Orientation of re-sliced data by using two angular measurements. (**b**) Data plot of 3D statistical measures (in the image of stereonets for the representation of 3D structural geological analysis).

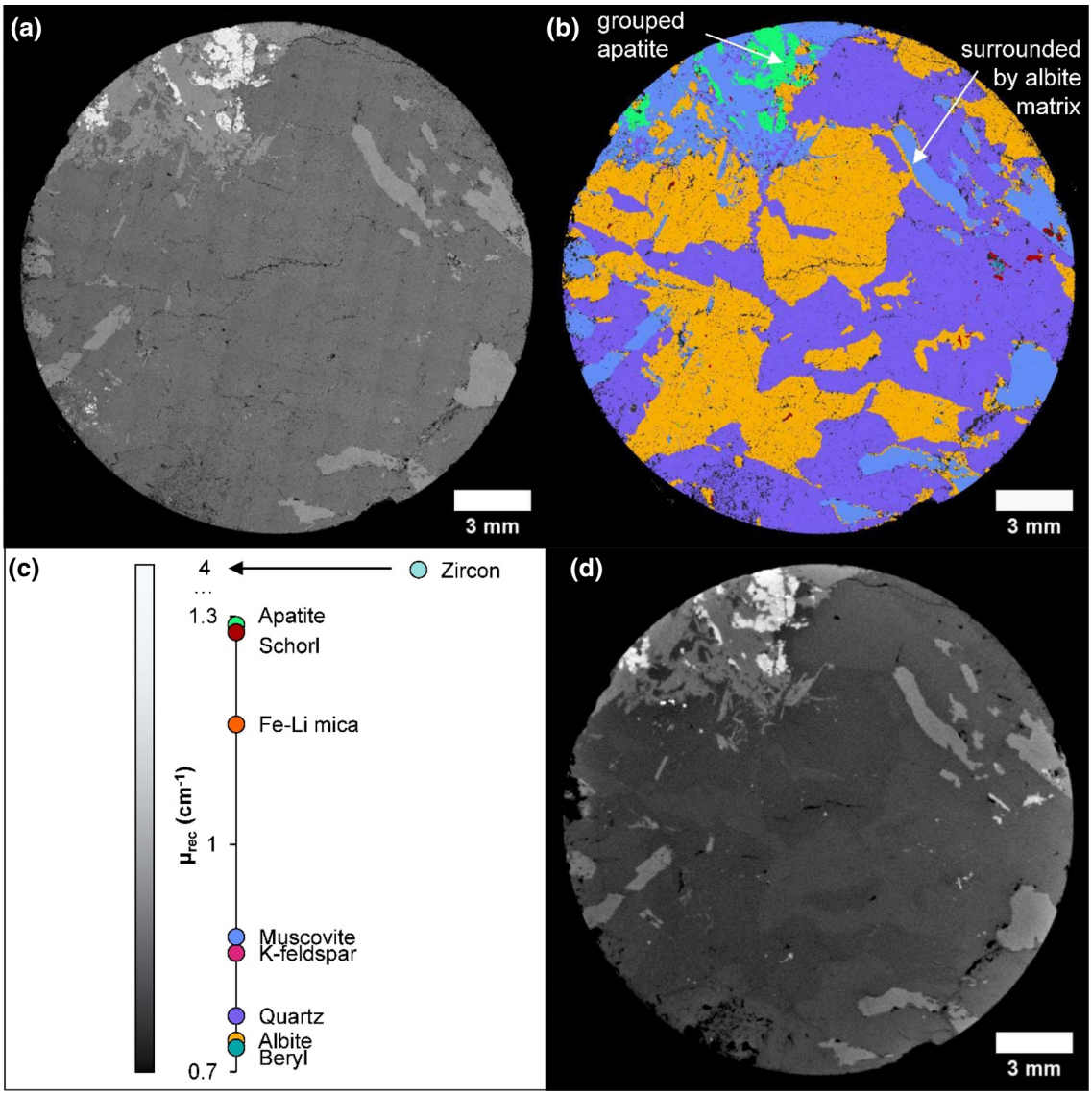

Figure 6. Mineral distribution map of sample A (acquired with TIMA-X) with the corresponding µCT slice. (**a**) BSE image. (**b**) Mineral distribution map. (**c**) Calculated μ_{rec} values for the identified (color coded) minerals in the mineral distribution map. (**d**) Corresponding µCT slice.

by the presence of muscovite fragments nor of the main matrix constituents. One remarkable observation was the presence of a two centimeter long schorl fragment crosscutting sample B (Fig. 8a and b). There were several mineral phases associated with this schorl crystal, which were, from low density to high density, albite–muscovite–schorl or at least minerals with a similar gray value. Because this was an important observation, sample B was re-polished to acquire an additional mineral distribution map for this slice to confirm the µCT observations. It is important to note that, next to albite, quartz was also identified as a low-density phase within this schorl crystal. The observed occurrence of a small barite vein as a possible mineral inclusion within a muscovite grain during TIMA-X analysis was confirmed to be a real mineral inclusion during µCT analyses.

Segmentation of Mineral Phases

Based on the observations acquired for the two samples and the predetermined μ_{rec} values (Fig. 2b),

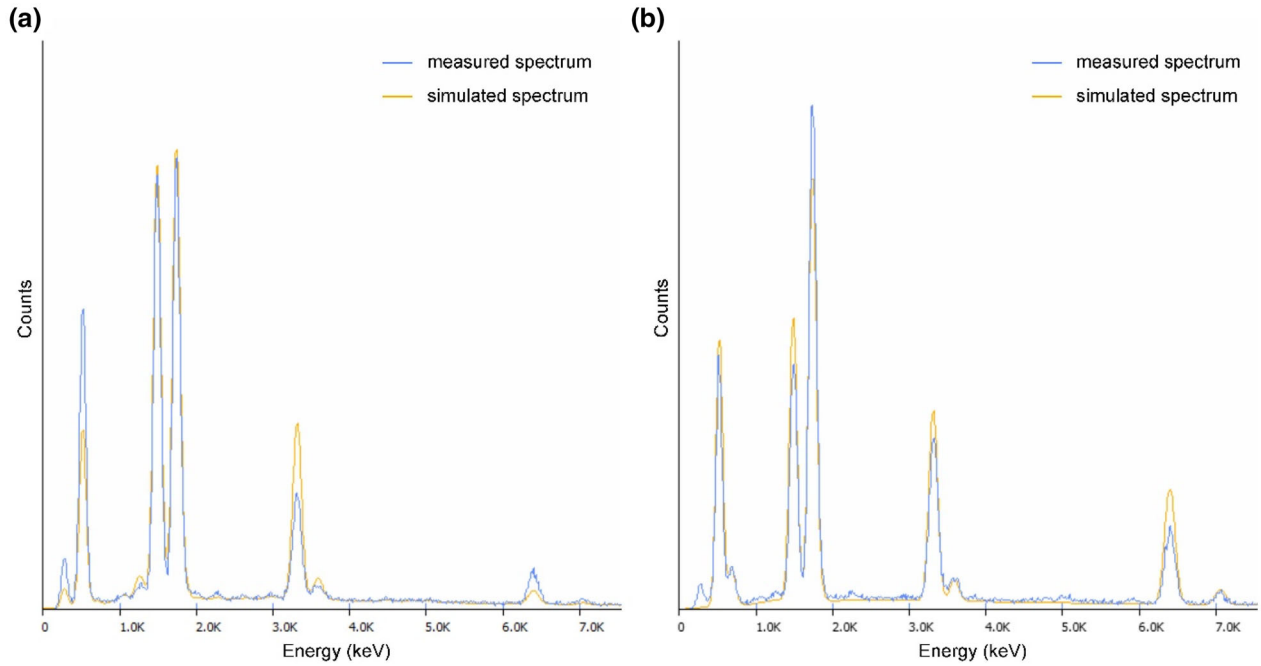

Figure 7. Comparison of measured and simulated EDX spectra of (**a**) muscovite and (**b**) minerals that classify as Fe–Li mica (zinnwaldite) following the AM system.

different phases were selected for segmentation using the proposed methodology. An example of a possible output for sample A is presented below.

The group of identified mineral phases was reduced to the following five segmented phases (from low to high μ_{rec}): albite, quartz, muscovite, schorl/apatite and dense mineral phases (Fig. 9), with vol% of 43.51, 43.43, 11.36, 1.60 and 0.04, respectively, with respect to the sample data after a first step of data preparation. The remaining 0.06 vol% was removed from the dataset through post-processing to remove false mineral phase identification at the boundaries between two segmented phases. The difference in grayscale value and μ_{rec} of schorl and apatite were limited. Apatite was expected to be only slightly higher in grayscale value (see Fig. 2b) and were therefore grouped because of their similarity. The dense mineral phase consisted of all identified mineral phases for which μ_{rec} was higher than the other segmented phases (i.e., denser than schorl/apatite). These phases included ore minerals and high-density accessory minerals (in particular zircon) that were observed during mineral mapping. It must be noted that this sample was also re-polished to chemically investigate the largest grain that was classified as a dense mineral phase using TIMA-X (Fig. 9). It, however, displayed relatively higher grayscale values, and thus higher μ_{rec} value, than zircon. This grain has been identified as a Nb–Ta–U oxide mineral and indeed not as zircon. This Nb–Ta–U oxide, or previously described in Lehmann et al. (2008) as U-rich microlite, is one of the more rare Nb–Ta minerals present in the mineralized pegmatites, compared to the more common columbite–tantalite solid-solution series. However, this mineral could be locally concentrated in specific zones (Lehmann et al., 2008), and has been described to be characteristic for the Nb–Ta mineralization of the Gatumba area (Melcher et al., 2015).

Interrelationships and Orientation of Mineral Phases

Sample A presented in the previous section was analyzed further using a correlation matrix (Fig. 10) to investigate possible spatial correlations. For the five different segmented phases, 10 unique interrelationships could be calculated. The coefficient of variation (Fig. 11) was calculated for the five different segmented phases, which may give insights into the possible preferential orientation of minerals to deduce possible oriented growth or the so-called

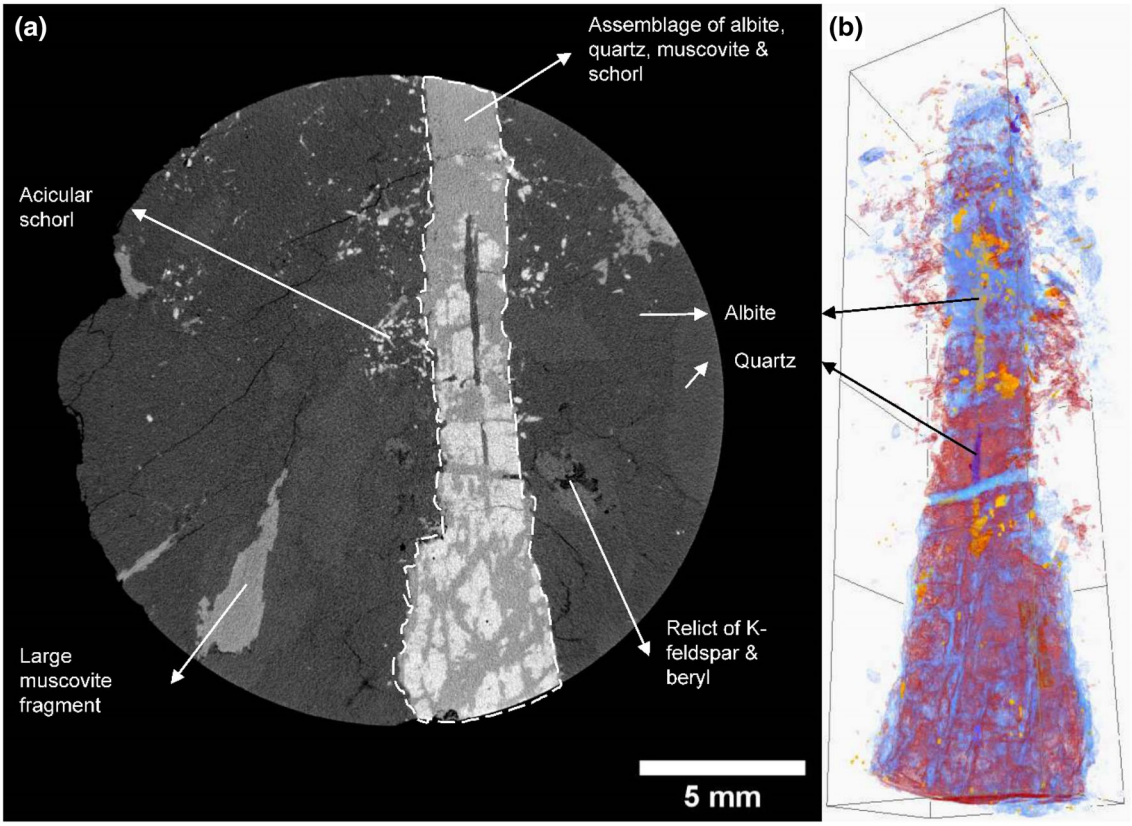

Figure 8. (**a**) A μCT slice of sample B with some of the most important identified mineral phases indicated. Note that the grayscale values are adjusted to the range of values present within this slice (see Fig. 6c for relative position of μ_{rec} for each indicated mineral). (**b**) 3D visualization of the elongated assemblage of albite, quartz, muscovite, and schorl in (**a**) and where the different phases are indicated according to their colors used in Figure 6 (grid size = 5 mm).

unidirectional solidification texture (UST) (Shannon et al., 1982). One of the main observations from Figure 10 was the omnidirectional strong negative correlation between albite and quartz, which was to a lesser extent also observable between albite and muscovite. However, an omnidirectional positive correlation was observed between schorl/apatite and the dense mineral phase, which was here mostly zircon. In data plots of the correlation matrix where muscovite was considered (Fig. 10), the correlation was influenced strongly by the coefficient of variation of muscovite (Fig. 11). Mostly low c_v values at an inclination of 90° were reflected particularly in the correlation between muscovite and schorl/apatite and between muscovite and the dense mineral phase. The same was observed for c_v values of the dense mineral phase, where the deviating value at an azimuth of 90° and inclination of 45° was well reflected in the correlation matrix involving the dense mineral phase. A relatively high c_v value at this orientation can be explained by the large Nb–Ta–U oxide grain (see Fig. 11) included within the group of otherwise much smaller dense mineral grains. The influence of c_v was less pronounced for albite and quartz because both phases only displayed low c_v values within small ranges (0.154–0.45 and 0.127–0.372, respectively).

DISCUSSION

The combination of different imaging techniques, both 2D and 3D, has a strong application potential for the analysis of mineralogy and geochemistry of rock samples down to the microscopic scale. Extending this into 3D allows for the study of mineral relationships and the quantification of morphological characteristics of minerals without stereological errors from 2D estimations. Recent existing practices in analyzing ore samples (e.g.,

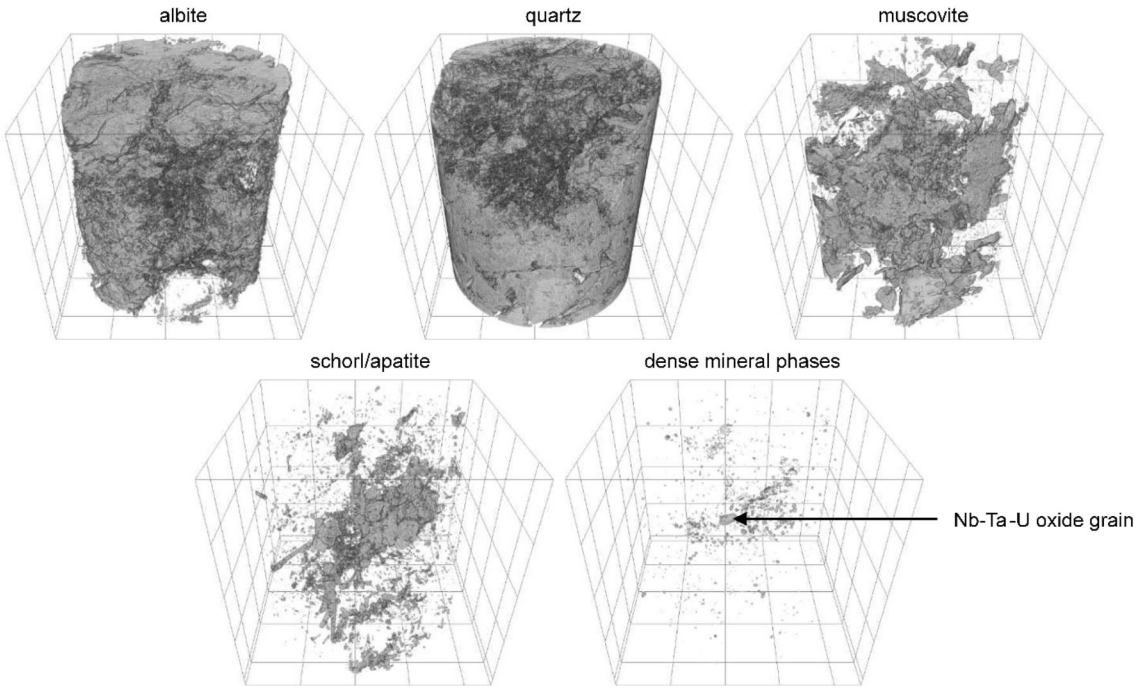

Figure 9. Volume rendering of the different segmented phases within sample A (grid size = 5 mm).

Guntoro et al., 2019b; Warlo et al., 2021) demonstrate both the shortcomings as well as the benefits from combining SEM–EDX with μCT.

Polished sections were analyzed here with SEM–EDX to classify minerals with an AM system and the obtained mineral distribution maps were used to interpret their distribution in 3D. Sample preparation was especially necessary to perform SEM-based AM analyses, as this technique requires a well-polished surface with a sputtered carbon coating to produce high quality images (Reed, 2005). Besides, commercial SEM instrumentation often comes with standard sample holders, which limits the possible 3D volumes to be analyzed with both SEM and μCT. For our system, the diameter per sample was standard one inch and the sample was also limited in height to fit in the vacuum chamber. In addition, when scanning polished samples with μCT, image artifacts occur at the surface of samples due to the so-called cone-beam effect (Cnudde & Boone, 2013; Guntoro et al., 2019b). This effect eventually alters the grayscale values and thus also limits the possible segmentation. To anticipate these, core samples with the same diameter, but extended in length, were scanned prior to any sample preparation. This allowed us to select a region of interest from the μCT data, in accordance with the polished sample, without having these image artifacts at the polished surfaces. By doing this, the information from an equivalent μCT slice of the polished surface can then be used to train the 3D Weka segmentation. Alternatively, optimized image acquisition (De Witte, 2010) and post-processing steps (Kazhdan et al., 2015) can be undertaken to remove some of these image artifacts at the surface of samples.

Despite the above-mentioned limitations of combining μCT with SEM–EDX, a SEM–EDX based AM system proved to be an important and needed part of the methodology to provide background information for visual interpretation and/or segmentation of μCT data. SEM-based AM systems are commercially more and more well-established (Graham, 2017) and they are increasingly applied in geological studies (e.g., Warlo et al., 2019; Keulen et al., 2020). For minerals with similar chemical compositions, but with different crystalline structures (e.g., hematite and magnetite) or minerals that are not straightforward to classify using existing SEM-based AM systems (e.g., mineral polymorphs), one can consider XRD. XRD is a routinely performed, but destructive, laboratory technique that

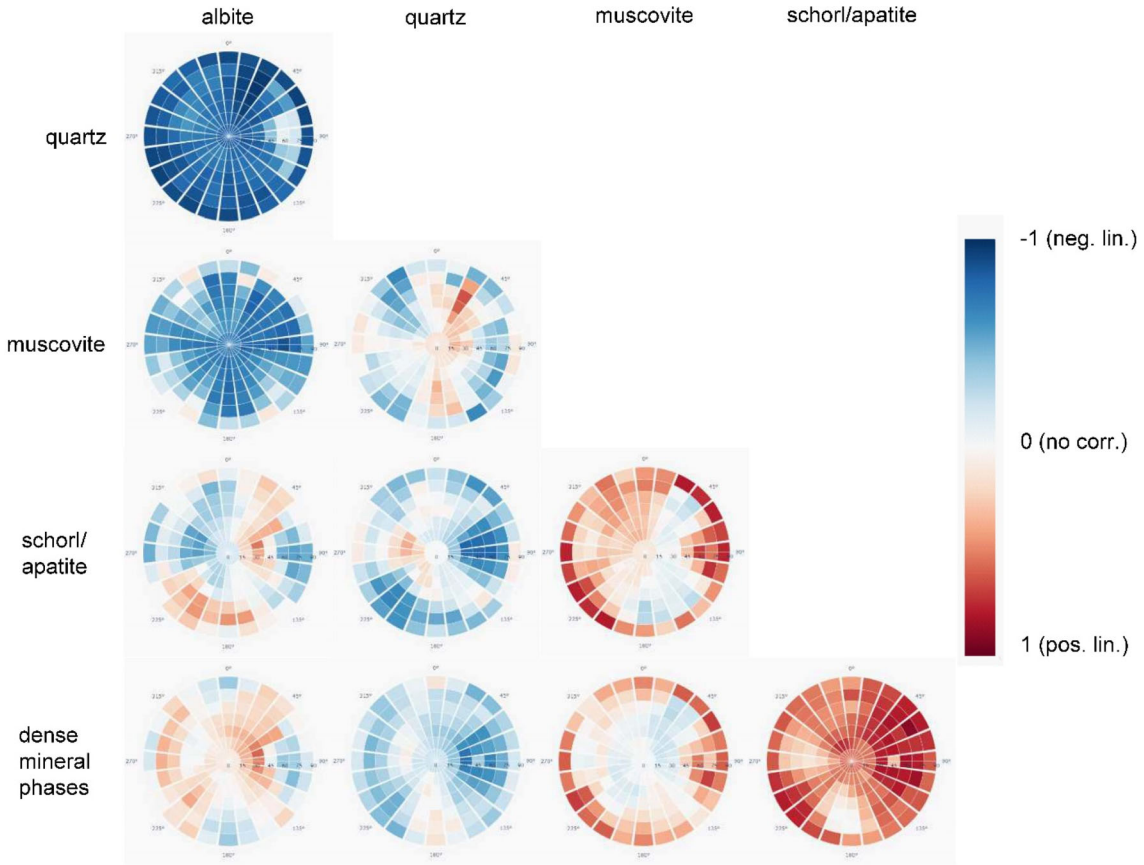

Figure 10. Correlation matrix of the different segmented phases within sample A (see Fig. 9).

has already proven to be an essential tool for phase identification within geosciences (Artioli, 2018). Advanced developments in X-ray microscopy enabled the establishment of laboratory-based diffraction contrast tomography (Holzner et al., 2016), which opens opportunities for further research in 3D materials science. An example, where this could have been of benefit here, is the identification of a mineral that strongly resembled biotite in EDX spectrum (Fig. 7b), but which showed to have a density that was too low and, therefore, was classified as a Fe–Li mica. Although the Li-content of this mineral was not measurable with the used SEM equipment, as the elemental range of EDX is limited from beryllium to uranium, this chemical information can be inferred from the combination of SEM-based AM, µCT analyses and previous observations. Solely based on EDX spectra (Fig. 7b), this mineral can be interpreted as the iron end-member (annite) of the biotite mica group. However, the relative position of μ_{rec} in the µCT images shows that its value is too low to be classified as biotite. The calculated μ_{rec} was lower than those of apatite and schorl, which suggests the presence of a low atomic number element that significantly lowers its attenuation coefficient. Lithium is such an element that is known to be incorporated into mica minerals of corresponding pegmatites (Hulsbosch et al., 2013). Lepidolite and zinnwaldite, respectively, containing 3.70–5.42 wt% and 2.19–3.72 wt% of Li_2O (Anthony et al., 2001), are the two most common Li-micas in cassiterite and topaz-bearing pegmatites (Dill, 2010) and were previously also observed in this mineralization (Hulsbosch et al., 2013). The relative position of μ_{rec} matched well with the simulated μ_{rec} value of zinnwaldite (Fig. 2b) and excluded lepidolite (μ_{rec} of lepidolite is too low). In this case, even powder XRD analysis would not give a decisive answer due to its resemblance with other mica minerals, especially when the co-existence of other micas is

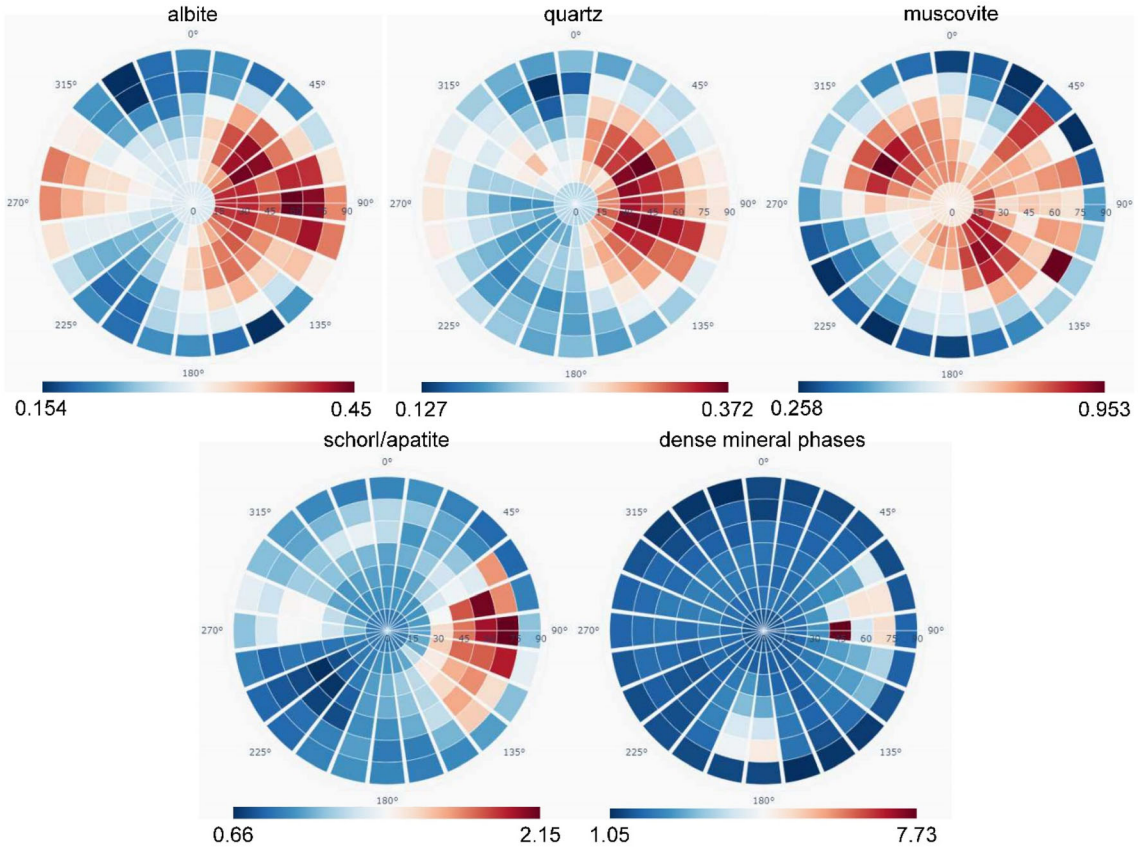

Figure 11. Coefficients of variation for segmented phases of sample A (see Fig. 9). Note that each segmented mineral phase displays a different range of values.

inevitable in the sample preparation. Only chemical data from, e.g., laser ablation inductively coupled plasma mass spectrometry can give a decisive answer, but techniques like this are often not available or are too costly for routinely analyses.

By using XRD analysis, it would have been possible to narrow the possibilities down to a more specific mineral or mineral group. Although this may be of importance for the mineralogical interpretation of the data, this will hardly influence the segmentation of the μCT data. For the example of hematite (Fe_2O_3; ρ = 5.23 g/cm^3) and magnetite ($Fe^{2+}Fe_2O_4$; ρ = 5.20 g/cm^3), μ_{rec} will be here nearly the same (2.81 and 2.83, respectively).

The main advantage of mineral distribution maps acquired with TIMA-X is the possibility to correlate this 2D mineralogical information directly with a 3D μCT dataset and to re-polish the sample to a specific section of interest for verification. As an example, the mineral assemblage in Figure 8 was checked to see if the assumptions that were made from μCT images were correct. It is the interpretation of these sought for 3D mineral assemblages that will help to further refine the paragenesis of ore deposits. On top of that, similar to a mineral standards library that is built within AM systems, a list of identified minerals can be deduced to build a library of linear attenuation coefficients μ_{lin} (see Fig. 2a). Once all possible minerals encountered for the ore deposit under consideration are known, a library of μ_{rec} values can be calculated for a given μCT setup. It is just so that calculations of the linear attenuation coefficient μ_{lin} are not sufficient to predict the behavior, or better the produced grayscale values, of the different minerals in the μCT images. As visualized in Figure 2a, this value depends largely on the energy of radiation. Because the source of radiation is almost always polychromatic in laboratory-based systems (Cnudde & Boone, 2013), combined with an energy-dependent detector sensitivity, a measure

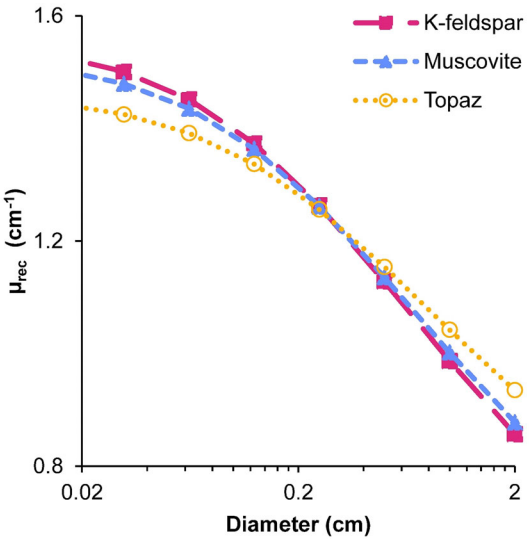

Figure 12. Extreme example of the influence of material composition and sample thickness on the relative position of μ_{rec} for three minerals that were encountered during SEM–EDX analyses.

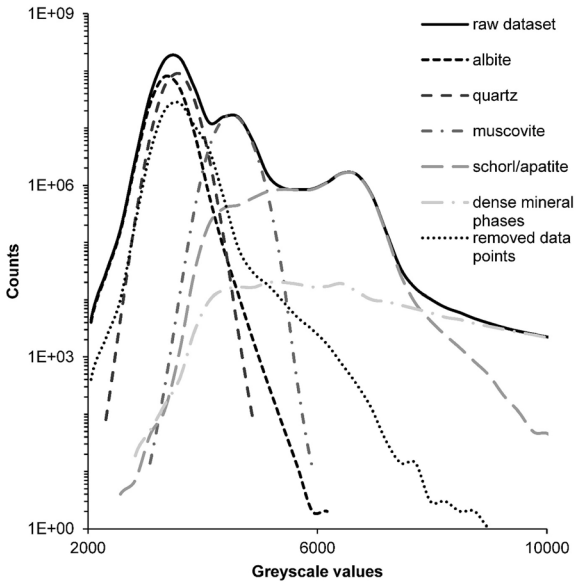

Figure 13. Distributions of grayscale values for each segmented phase in sample A. The eroded data points coincide with local maxima at the intersection between two segmented phases.

needs to be calculated for a certain setup. A possibility is to calculate this based on the effective energy (Bam et al., 2020), which is a weighted average of an actual polychromatic beam for a specific voltage and setup (see Table 1). This was successfully applied in recent studies (Gibson et al., 2021; Warlo et al., 2021). Although this assumption may be correct when considering the X-ray beam before entering the sample, this X-ray beam is still a polychromatic beam that will be altered in terms of effective energy depending on material composition and sample thickness. As also issued in Bam et al. 2020, this will affect the expected discrimination between the minerals (see Fig. 12). To counter this issue, the effect of material properties and sample thickness and the full polychromatic beam was here taken into account to calculate μ_{rec} for each mineral (Fig. 2b). The μ_{rec} was calculated here on the assumption that a monomineralic sample with a thickness of 2 cm (according to the used sample diameter in this study) was scanned. Note that although these values proved to serve as perfect guides for phase segmentation, images are still prone to several systematic errors (e.g., noise, discretization effects, imaging artifacts; Cnudde & Boone, 2013). Machine learning tools like Weka 3D segmentation (Arganda-Carreras et al., 2017) are capable of dealing with some of these errors to improve the accuracy of the segmented phases. By training a range of image features (e.g., edge detectors and texture filters) it becomes possible to distinguish different phases from each other that may contain overlapping grayscale values (Fig. 13). Extending mineral phase segmentation to more advanced machine learning techniques could provide even better results (e.g., Furat et al., 2019; Evsevleev et al., 2020), but would require a more elaborate period of segmentation training.

The resulting segmented data can be quantified in 3D through a variation of data analysis methods (Guntoro et al., 2019a) to open up a new depth of information in describing textures of minerals. This allows for the 3D interpretation of both the individual phases and of the interrelationships between the different phases. In terms of ore geology, textural elements like size, shape, and orientation of mineral grains are referred to as structural textures, while the spatial relation between mineral phases is referred to as stationary texture (Lobos et al., 2016). The presented methodology covers both the quantitative extraction of structural textures (i.e., coefficient of variation as a measure of orientation; Fig. 11) and stationary textures (i.e., correlation matrix; Fig. 10) with low computational expense. The employed script only required to open the segmented dataset four times at the same time: (± 7 GB). Because this feature extraction does not take into account individual grains/minerals for its calculations, this could be applied immediately to

single/grouped grayscale values instead of more elaborately trained segmented datasets. The extraction of these features in such a manner opens possibilities to quantify datasets of whole core sections and/or of selected segments within these cores (e.g., vein orientation and correlation of mineral phases with ore minerals). As an example, one Nb–Ta–U oxide and multiple zircon grains were found to be associated with a stellate aggregate of muscovite that was strongly intergrown with a grouped occurrence of apatite (see Fig. 6b). It is this spatial association that caused the positive correlation between schorl/apatite and the dense mineral phase (Fig. 10).

CONCLUSIONS

In this work, we applied a comprehensive methodology for characterization of the mineralogy of a Sn–Nb–Ta mineralization in 3D. First, a mineral library of all minerals present was derived from SEM-based AM analyses for the calculation of μ_{lin}. The deduced μ_{rec} served as a most correct guide to differentiate between different minerals for a given experimental μCT setup. For example, this allowed us to differentiate biotite from a Fe–Li mica due to the attribution of the low atomic element lithium. The trainable Weka 3D segmentation within the open-software Fiji environment allowed for data preparation and the differentiation between five separate phases (albite, quartz, muscovite, schorl/apatite and dense mineral phase). Quantitative information on the orientation of individual mineral phases and their spatial correlation in 3D was provided by the calculation of statistical descriptors at a low computational expense. Combining μCT and an SEM-based AM system within a comprehensive methodology can aid in the mineralogical investigation of an ore deposit, both in aspects of visualization and quantification at the microscopic scale.

ACKNOWLEDGMENTS

This work is funded by the European Electron and X-ray Imaging Infrastructure (EXCITE), this project has received funding from the European Union's Horizon 2020 research and innovation programme under grant agreement No 101005611. SEM instrumentation has received funding from Research Foundation – Flanders (FWO) for medium-scale research infrastructure under grant agreement number I013118N.

DECLARATIONS

Conflict of Interest The authors declare that they have no known competing financial interests or personal relationships that could have appeared to influence the work reported in this paper.

REFERENCES

Ali, S. H., Giurco, D., Arndt, N., Nickless, E., Brown, G., Demetriades, A., Durrheim, R., Enriquez, M. A., Kinnaird, J., Littleboy, A., Meinert, L. D., Oberhänsli, R., Salem, J., Schodde, R., Schneider, G., Vidal, O., & Yakovleva, N. (2017). Mineral supply for sustainable development requires resource governance. *Nature, 543*, 367–372.

Anthony, J. W., Bideaux, R. A., Bladh, K. W., & Nichols M. C. (eds.), (2001). *Handbook of mineralogy*. Mineralogical Society of America. http://www.handbookofmineralogy.org/.

Arganda-Carreras, I. (2018). *Weka Segmentation tiling script*. Scientific Community Image Forum. https://forum.image.sc/t/trainable-wekaerror-large-images/10929.

Arganda-Carreras, I., Kaynig, V., Rueden, C., Eliceiri, K. W., Schindelin, J., Cardona, A., & Sebastian Sueng, H. (2017). Trainable Weka Segmentation: A machine learning tool for microscopy pixel classification. *Bioinformatics, 33*(15), 2424–2426.

Artioli, G. (2018). X-ray diffraction, studies of inorganic compounds and minerals. *Encyclopedia of Spectroscopy and Spectrometry, 3*, 676–683.

Bam, L. C., Miller, J. A., & Becker, M. (2020). A mineral X-ray linear attenuation coefficient tool (MXLAC) to assess mineralogical differentiation for X-ray computed tomography scanning. *Minerals, 10*, 441.

Becker, M., Jardine, M. A., Miller, J. A., & Harris, M. (2016). X-ray computed tomography—A geometallurgical tool for 3D textural analysis of drill core? In S. Dominy & L. O'Connor (Eds.), *The third AusIMM international geometallurgy conference 2016* (pp. 231–240). AusIMM.

Callow, B., Falcon-Suarez, I., Moreno-Marin, H., Bull, J. M., & Ahmed, S. (2020). Optimal X-ray micro-CT image based methods for porosity and permeability quantification in heterogeneous sandstones. *Geophysical Journal International, 223*(2), 1210–1229.

Chantler, C. T., Olsen, K., Dragoset, R. A., Chang, J., Kishore, A. R., Kotochigova, S. A., & Zucker, D. S. (2005). *X-ray form factor, attenuation and scattering tables (version 2.1)*. National Institute of Standards and Technology.

Cnudde, V., & Boone, M. N. (2013). High-resolution X-ray computed tomography in geosciences: A review of the current technology and applications. *Earth-Science Reviews, 123*, 1–17.

De Boever, W., Derluyn, H., Van Loo, D., Van Hoorebeke, L., & Cnudde, V. (2015). Data-fusion of high resolution X-ray CT, SEM and EDS for 3D and pseudo-3D chemical and structural characterization of sandstone. *Micron, 74*, 15–21.

De Witte, Y. (2010). *Improved and Practically Feasible Reconstruction Methods for High Resolution X-ray Tomography*.

(Doctoral dissertation, Ghent University, Ghent). Retrieved from http://lib.ugent.be/catalog/rug01:001404410.

Dewaele, S., Henjes-Kunst, F., Melcher, F., Sitnikova, M., Burgess, R., Gerdes, A., Fernandez, M. A., De Clercq, F., Muchez, P., & Lehmann, B. (2011). Late Neoproterozoic overprinting of the cassiterite and columbite-tantalite bearing pegmatites of the Gatumba area, Rwanda (Central Africa). *Journal of African Earth Sciences, 61*(1), 10–26.

Dhaene, J., Pauwels, E., De Schryver, T., De Muynck, A., Dierick, M., & Van Hoorebeke, L. (2015). A realistic projection simulator for laboratory based X-ray micro-CT. *Nuclear Instruments and Methods in Physics Research B, 342*, 170–178.

Dill, H. G. (2010). The ''chessboard'' classification scheme of mineral deposits: Mineralogy and geology from aluminum to zirconium. *Earth-Science Reviews, 100*, 1–420.

Evsevleev, S., Paciornik, S., & Bruno, G. (2020). Advanced deep learning-based 3D microstructures characterization of multiphase metal matrix composites. *Advanced Engineering Materials, 22*, 1901197.

Furat, O., Wang, M., Neumann, M., Petrich, L., Weber, M., Krill, C. E., III., & Schmidt, V. (2019). Machine learning techniques for the segmentation of tomographic image data of functional materials. *Frontiers in Materials, 6*, 145.

Gessner, K., Blenkinsop, T., & Sorjonen-Ward, P. (2018). Characterization of ore-forming systems—Advances and challenges. In K. Gessner, T. G. Blenkinsop, & P. Sorjonen-Ward (Eds.), *Geological Society, London, Special Publications* (Vol. 453, pp. 1–6). Geological Society of London.

Gibson, B., Nwaila, G., & Petersen, J. (2021). Characterization of a coarse synthetic silver ore as a model ore material for heap leaching research. *Minerals Engineering, 174*, 107253.

Godel, B. (2013). High-resolution X-ray computed tomography and its application to ore deposits: From data acquisition to quantitative three-dimensional measurements with case studies from Ni–Cu-PGE deposits. *Economic Geology, 108*(8), 2005–2019.

Graham, S. D. (2017). Automated mineralogy—The past, present and future. In F. Kongoli, D. Bradshaw, K. Waters, J. Starkey, & A. C. Silva (Eds.), *Sustainable Industrial Processing Summit SIPS 2017* (Vol. 4, pp. 96–115). Flogen Star Outreach.

Gu, L., Wang, N., Tang, X., & Changela, H. G. (2020). Application of FIB-SEM techniques for the advanced characterization of earth and planetary materials. *Scanning, 2020*, 8406917.

Guntoro, P. I., Ghorbani, Y., Koch, P.-H., & Rosenkranz, J. (2019a). X-ray microcomputed tomography (μCT) for mineral characterization: A review of data analysis methods. *Minerals, 9*(3), 183.

Guntoro, P. I., Tiu, G., Ghorbani, Y., Lund, C., & Rosenkranz, J. (2019b). Application of machine learning techniques in mineral phase segmentation for X-ray microcomputed tomography (μCT) data. *Minerals Engineering, 142*, 105882.

Hayes, S. M., & McCullough, E. A. (2018). Critical minerals: A review of elemental trends in comprehensive criticality studies. *Resources Policy, 59*, 192–199.

Holzner, C., Lavery, L., Bale, H., Merkle, A., McDonald, S., Withers, P., Zhang, Y., Juul Jensen, D., Kimura, M., Lyckegaard, A., Reischig, P., & Lauridsen, E. M. (2016). Diffraction contrast tomography in the laboratory applications and future directions. *Microscopy Today, 24*(4), 34–43.

Hrstka, T., Gottlieb, P., Skála, R., Breiter, K., & Motl, D. (2018). Automated mineralogy and petrology—Applications of TESCAN Integrated Mineral Analyzer (TIMA). *Journal of Geosciences, 63*, 47–63.

Hulsbosch, N., Hertogen, J., Dewaele, S., Andre, L., & Muchez, P. (2013). Petrographic and mineralogical characterisation of fractionated pegmatites culminating in the Nb–Ta–Sn pegmatites of the Gatumba area (western Rwanda). *Geologica Belgica, 16*(1–2), 105–117.

Hulsbosch, N., & Muchez, P. (2020). Tracing fluid saturation during pegmatite differentiation by studying the fluid inclusion evolution and multiphase cassiterite mineralization of the Gatumba pegmatite dyke system (NW Rwanda). *Lithos, 354–355*, 105285.

Jardine, M. A., Miller, J. A., & Becker, M. (2018). Coupled X-ray computed tomography and grey level co-occurrence matrices as a method for quantification of mineralogy and texture in 3D. *Computers and Geosciences, 111*, 105–117.

Kazhdan, M., Lillaney, K., Roncal, W., Bock, D., Vogelstein, J., & Burns, R. (2015). Gradient-domain fusion for color correction in large EM image stacks.

Ketcham, R. A., & Mote, A. S. (2019). Accurate measurement of small features in X-ray CT data volumes, demonstrated using gold grains. *Journal of Geophysical Research: Solid Earth, 124*, 3508–3529.

Keulen, N., Malkki, S. N., & Graham, S. (2020). Automated quantitative mineralogy applied to metamorphic rocks. *Minerals, 10*, 47.

Kyle, J. R., & Ketcham, R. A. (2015). Application of high resolution X-ray computed tomography to mineral deposit origin, evaluation, and processing. *Ore Geology Reviews, 65*(4), 821–839.

Laforce, B., Vermeulen, B., Garrevoet, J., Vekemans, B., Van Hoorebeke, L., Janssen, C., & Vincze, L. (2016). Laboratory scale X-ray fluorescence tomography: Instrument characterization and application in earth and environmental science. *Analytical Chemistry, 88*(6), 3386–3391.

Lehmann, B., Halder, S., Ruzindana Munana, J., Ngizimana, J., & Biryabarema, M. (2014). The geochemical signature of rare-metal pegmatites in Central Africa: Magmatic rocks in the Gatumba tin-tantalum mining district, Rwanda. *Journal of Geochemical Exploration, 144*, 528–538.

Lehmann, B., Melcher, F., Sitnikova, M. A., & Ruzindana, M. J. (2008). The Gatumba rare-metal pegmatites: Chemical signature and environmental impact. *Études Rwandaises, 16*, 25–40.

Lobos, R., Silva, J. F., Ortiz, J. M., Díaz, G., & Egaña, A. (2016). Analysis and classification of natural rock textures based on new transform-based features. *Mathematical Geosciences, 48*(7), 835–870.

Masschaele, B., Dierick, M., Van Loo, D., Boone, M. N., Brabant, L., Pauwels, E., Cnudde, V., & Van Hoorebeke, L. (2013). HECTOR: A 240 kV micro-CT setup optimized for research. *Journal of Physics: Conference Series, 463*, 012012.

Melcher, F., Graupner, T., Gäbler, H.-E., Sitnikova, M., Henjes-Kunst, F., Oberthür, T., Gerdes, A., & Dewaele, S. (2015). Tantalum-(niobium-tin) mineralisation in African pegmatites and rare metal granites: Constraints from Ta–Nb oxide mineralogy, geochemistry and U-Pb geochronology. *Ore Geology Reviews, 64*, 667–719.

Otsu, N. (1979). A threshold selection method from gray-level histograms. *IEEE Transactions on Systems, Man and Cybernetics, 9*(1), 62–66.

Pearce, M. A., Godel, B. M., Fisher, L. A., Schoneveld, L. E., Cleverley, J. S., Oliver, N. H. S., & Nugus, M. (2018). Microscale data to macroscale processes: A review of microcharacterization applied to mineral systems. In K. Gessner, T. G. Blenkinsop, & P. Sorjonen-Ward (Eds.), *Geological Society, London, Special Publications* (Vol. 453, pp. 7–39). Geological Society of London.

Reed, S. J. B. (2005). *Electron microprobe analysis and scanning electron microscopy in geology* (2nd ed.). Cambridge University Press.

Reuter, M. A., van Schaik, A., Gutzmer, J., Bartie, N., & Abadías-Llamas, A. (2019). Challenges of the circular economy: A

material, metallurgical, and product design perspective. *Annual Review of Materials Research, 49*, 253–274.

Reyes, F., Lin, Q., Udoudo, O., Dodds, C., Lee, P. D., & Neethling, S. (2017). Calibrated X-ray microtomography for mineral ore quantification. *Minerals Engineering, 110*, 122–130.

Schindelin, J., Arganda Carreras, I., Frise, E., Kaynig, V., Longair, M., Pietzsch, T., Preibisch, S., Rueden, C., Saalfeld, S., Schmid, B., Tinevez, J.-Y., White, D. J., Hartenstein, V., Eliceiri, K., Tomancak, P., & Cardona, A. (2012). Fiji: An open-source platform for biological-image analysis. *Nature Methods, 9*, 676–682.

Shannon, J. R., Walker, B. M., Carten, R. B., & Geraghty, E. P. (1982). Unidirectional solidification textures and their significance in determining relative ages of intrusions at the Henderson Mine, Colorado. *Geology, 10*(6), 293–297.

Strzelecki, P. J., Świerczewska, A., Kopczewska, K., Fheed, A., Tarasiuk, J., & Wroński, S. (2021). Decoding rocks: An assessment of geomaterial microstructure using X-ray microtomography, image analysis and multivariate statistics. *Materials, 14*, 3266.

Vlassenbroeck, J., Dierick, M., Masschaele, B., Cnudde, V., Van Hoorebeke, L., & Jacobs, P. (2007). Software tools for quantification of X-ray microtomography at the UGCT. *Nuclear Instruments and Methods in Physics Research A, 580*(1), 442–445.

Wang, Y., & Miller, J. D. (2020). Current developments and applications of micro-CT for the 3D analysis of multiphase mineral systems in geometallurgy. *Earth-Science Reviews, 211*, 103406.

Warlo, M., Bark, G., Wanhainen, C., Butcher, A. R., Forsberg, F., Lycksam, H., & Kuva, J. (2021). Multi-scale X-ray computed tomography analysis to aid automated mineralogy in ore geology research. *Frontiers in Earth Science, 9*, 789372.

Warlo, M., Wanhainen, C., Bark, G., Butcher, A. R., McElroy, I., Brising, D., & Rollinson, G. K. (2019). Automated quantitative mineralogy optimized for simultaneous detection of (precious/critical) rare metals and base metals in a production-focused environment. *Minerals, 9*, 440.

Wellmer, F.-W., Buchholz, P., Gutzmer, J., Hagelüken, C., Herzig, P., Littke, R., & Thauer, R. K. (2019). *Raw materials for future energy supply*. Springer.